The Planetary Science Journal, 1:69 (11pp), 2020 December https://doi.org/10.3847/PSJ/abbe0c

On the Long-term Weathering of Airless Body Surfaces by the Heavy Minor Ions of the Solar Wind: Inputs from Ion Observations and SRIM Simulations

Quentin Nénon[1,2], and Andrew R. Poppe[1,2]
[1] Space Sciences Laboratory, University of California at Berkeley, 7 Gauss Way, Berkeley CA 94720, USA; nenon@berkeley.edu
[2] Solar System Exploration Research Virtual Institute, NASA Ames Research Center, Moffett Boulevard, Mountain View CA 94035, USA
Received 2020 June 23; revised 2020 September 11; accepted 2020 October 1; published 2020 December 3

Abstract

The importance of solar wind minor ions heavier than alpha particles in weathering airless body surfaces is an open debate. The fundamental question at stake is whether the variety of different minor ion species, their high masses, and their high charge states may overcome their low densities in the solar wind to enable them to significantly contribute to ion weathering processes. Here, long-term effects that develop on geological timescales are investigated. To do so, the long-term averaged energy spectrum of thermal and suprathermal solar wind ions is estimated by compiling and contrasting ion measurements gathered by the Advanced Composition Explorer (ACE), Wind, Solar TErrestrial RElations Observatory (STEREO), ARTEMIS, and Mars Atmosphere and Volatile Evolution (MAVEN) missions. The long-term ion environment is then convolved with Stopping and Range of Ions in Matter simulations. Combining these data and models, we find that solar wind minor ions significantly alter airless body surfaces, as they contribute to 8%–14% of the total sputtering and create 20%–50% of atomic displacements at depths greater than 100 nm. The new approach presented in this article therefore confirms that solar wind minor ions play an important role in the ion weathering of airless surfaces throughout the solar system.

Unified Astronomy Thesaurus concepts: Solar wind (1534); Lunar composition (948); The Moon (1692); Dwarf planets (419); Planetary surfaces (2113); Lunar surface (974); Surface processes (2116)

Supporting material: data behind figure

1. Introduction

1.1. Interplanetary Ions Alter Airless Body Surfaces over Long Timescales

Positively charged ions that travel in interplanetary space impact the surfaces of all airless bodies that are not protected by a large-scale magnetic field or thick atmosphere, i.e., the Moon, the moons of Mars, dwarf planets, asteroids, and comets. These ions alter the properties and composition of the surface regolith grains via a variety of physical processes, including (1) the contamination by exogenous atoms implanted by ions (Hashizume et al. 2000; Ozima et al. 2005; Grimberg et al. 2006; Terada et al. 2017), (2) the creation of optically opaque particles (Loeffler et al. 2009; Pieters & Noble 2016), and (3) the collisional displacement of material atoms. Optically opaque particles and atomic displacements darken and redden the near-infrared reflectance spectra of airless bodies (Brunetto & Strazzulla 2005; Marchi et al. 2005; Sanchez et al. 2012; Pieters & Noble 2016).

A first manifestation of ion-induced displacements is the sputtering of surface atoms and molecules into space. Ion sputtering is important as it generates exospheres around airless bodies (e.g., Wurz et al. 2010; Killen et al. 2012). In addition, sputtering alters the surface chemical composition, as the sputtering yield depends on the type of surface atom. This differential sputtering causes in particular a metallization of initially oxygen-rich surfaces (e.g., Szabo et al. 2018, 2020). Finally, sputtering ejects secondary ions that can possibly be detected to remotely characterize surface compositions (Elphic et al. 1991; Schaible et al. 2017).

The second effect linked to ion-induced atomic displacements is the development of structural defects up to the inducement of complete amorphization in initially crystalline material, including in particular the creation of amorphous rims that are 20–250 nm thick on lunar regolith grains (e.g., Dran et al. 1970; Bibring et al. 1972; Keller & McKay 1997; Christoffersen et al. 1996; Keller & Zhang 2015) and 30–100 nm thick on grains brought back from the asteroid Itokawa (Noguchi et al. 2014; Christoffersen & Keller 2015). Amorphous rims are observed to be thicker on some materials rather than others (e.g., plagioclase feldspar rims are typically thicker than olivine rims), and their thicknesses seem correlated with their exposure time to the solar wind (Keller & Zhang 2015 and references therein).

The content of exospheres sourced by ion sputtering is highly variable in time and linked to fast changes in the bombarding ion environment, for instance during the passage of a solar wind coronal mass ejection (Killen et al. 2012). However, both the compositional alteration induced by sputtering and the material amorphization occur on longer timescales ranging from years to millions of years, such that these processes depend on the bombarding ion environment averaged over long periods of time.

1.2. The Solar Wind is the Dominant Source of Interplanetary Ions

Airless bodies are impacted by a variety of ions, including GeV Galactic cosmic-ray ions (e.g., Adriani et al. 2011), singly charged pickup ions created from the neutral interstellar medium that enter the solar system (e.g., Möbius et al. 1985; Kollmann et al. 2019), and ions escaping planetary atmospheres (e.g., Terada et al. 2017;

Table 1
Acronyms and References for the Considered Space Missions and Ion Instruments

Mission (Bold) or Instrument	Reference
ARTEMIS: Acceleration, Reconnection, Turbulence, and Electrodynamics of the Moon's interaction	Angelopoulos (2011)
ARTEMIS-ESA: ElectroStatic Analyzer	McFadden et al. (2008)
ARTEMIS-SST: Solid State Telescope	
MAVEN: Mars Atmosphere and Volatile Evolution Mission	Jakosky et al. (2015)
MAVEN-STATIC: SupraThermal And Thermal Ion Composition	McFadden et al. (2015)
MAVEN-SEP: Solar Energetic Particle experiment	Larson et al. (2015)
ACE: Advanced Composition Explorer	Stone et al. (1998)
ACE-SWICS: Solar Wind Ion Composition Spectrometer	Gloeckler et al. (1998)
ACE-ULEIS: Ultra-Low-Energy Isotope Spectrometer	Mason et al. (1998)
Wind (not an acronym)	Acuña et al. (1995)
Wind-SWICS: Solar Wind Ion Composition Spectrometers	Gloeckler et al. (1995)
Wind-STICS: SupraThermal Ion Composition Spectrometer	Gloeckler et al. (1995)
Wind-STEP: SupraThermal Energetic Particle	Von Rosenvinge et al. (1995)
STEREO: Solar TERrestrial RElations Observatory	Kaiser et al. (2008)
STEREO-PLASTIC: PLAsma and SupraThermal Ion Composition experiment	Galvin et al. (2008)
STEREO-SIT: Suprathermal Ion Telescope	Luhmann et al. (2005)

Nénon et al. 2019). However, the number density of ions encountered in most of the heliosphere is dominated by the solar wind plasma ejected away from the Sun.

Three populations of solar wind ions are generally defined depending on their kinetic energies. The thermal core population has a typical bulk velocity of around 400 km s^{-1} and therefore a kinetic energy of ~1 keV $nucleon^{-1}$. Suprathermal ions with kinetic energies up to around 10 keV $nucleon^{-1}$ appear to always be present in the solar wind (Gloeckler 2003; Fisk & Gloeckler 2008). Ions with kinetic energies higher than 10 keV $nucleon^{-1}$ may also be ubiquitous in the solar wind (Fisk & Gloeckler 2008), or the long-term averaged flux of this population may be dominated by ions transported by transient interplanetary coronal mass ejections and corotating interaction regions (Mewaldt et al. 2001).

At thermal energies, protons dominate the number density of solar wind ions (~97%), so that early studies of ion weathering neglected the effects of other ion species (see Szabo et al. 2018 and references therein for a detailed history). The importance of thermal alpha particles He^{++} which constitute 2%–6% of the solar wind density was later recognized, as alpha particles sputter and amorphize airless body surfaces more efficiently than protons (e.g., Carrez et al. 2002; Killen et al. 2012; Poppe et al. 2018; Szabo et al. 2018, 2020; Nénon et al. 2019) and significantly modify their near-infrared reflectance spectra (Loeffler et al. 2009). Ions heavier than alpha particles are present in the solar wind at trace densities and have high charge states: C^{4+-6+}, N^{5+-7+}, O^{6+-8+}, Ne^{7+-9+}, Mg^{7+-10+}, Si^{6+-12+}, S^{6+-11+}, Fe^{7+-14+} (Von Steiger et al. 2000).

The importance of solar wind minor ions with masses greater than alpha particles in the ion weathering of airless body surfaces is an open debate. Previous efforts have considered the sputtering effect of the thermal 1 keV $nucleon^{-1}$ ion population (Shemansky 2003; Kallio et al. 2008; Barghouty et al. 2011; Killen et al. 2012; Szabo et al. 2018, 2020). However, these studies rely on the assumption that sputtering is caused by a roughly monoenergetic beam of ions. The validity of this assumption on long timescales deserves to be verified, as the time variability of the solar wind bulk speed shifts the peak kinetic energy over time from 0.4 to 2 keV $nucleon^{-1}$ (Bochsler 2007).

Some experiments have shown the capability of very heavy ions to amorphize airless body material (Brunetto & Strazzulla 2005; Marchi et al. 2005). However, the results of these studies alone are not sufficient to discuss the importance for the amorphization process of minor ions compared to protons and alpha particles. Finally, suprathermal protons have been proposed by Poppe et al. (2018) to be the origin of amorphous rims thicker than the ~10–50 nm penetration depths of 1 keV $nucleon^{-1}$ ions. Similarly, the role of suprathermal minor ions of the solar wind in the long-term weathering of airless bodies has never been studied.

In this article, the importance of solar wind minor ions in the long-term sputtering and amorphization of airless body material is investigated by combining for the first time long-term averaged minor ion energy spectra with numerical simulations of their weathering effects. To do so, we compile and compare in Section 2 the long-term averaged kinetic energy spectra of ions observed by instruments on board the Advanced Composition Explorer (ACE), ARTEMIS, Mars Atmosphere and Volatile Evolution (MAVEN), Solar TErrestrial RElations Observatory (STEREO), and Wind missions. In Section 3, the best available estimate of the long-term averaged ion spectra is convolved with energy and species-dependent sputtering yields computed with the Stopping and Range of Ions in Matter (SRIM) software (Ziegler et al. 2013). SRIM simulations are also used in Section 4 to investigate the importance of minor ions in displacing atoms in the uppermost micrometer of airless body material.

2. The Long-term Averaged Kinetic Energy Spectra of Protons, Alphas, and Heavy Minor Ions

Table 1 defines the acronyms used hereafter for the names of space missions and charged particle instruments. Two types of charged particle instrument technologies are typically used to observe solar wind ions: electrostatic analyzers that can observe the thermal and suprathermal populations (up to typically a few tens of keV per charge), and systems that rely on solid state detectors (SSDs) to observe more energetic suprathermal ions (energies higher than tens of keV). These two technologies alone cannot identify the mass per charge and mass of ions. The determination of the two latter quantities is generally achieved by adding a measurement of the ion time of flight between two foils (to electrostatic analyzers and SSD-based systems) and/or the energy deposited in a solid state detector (to electrostatic analyzers).

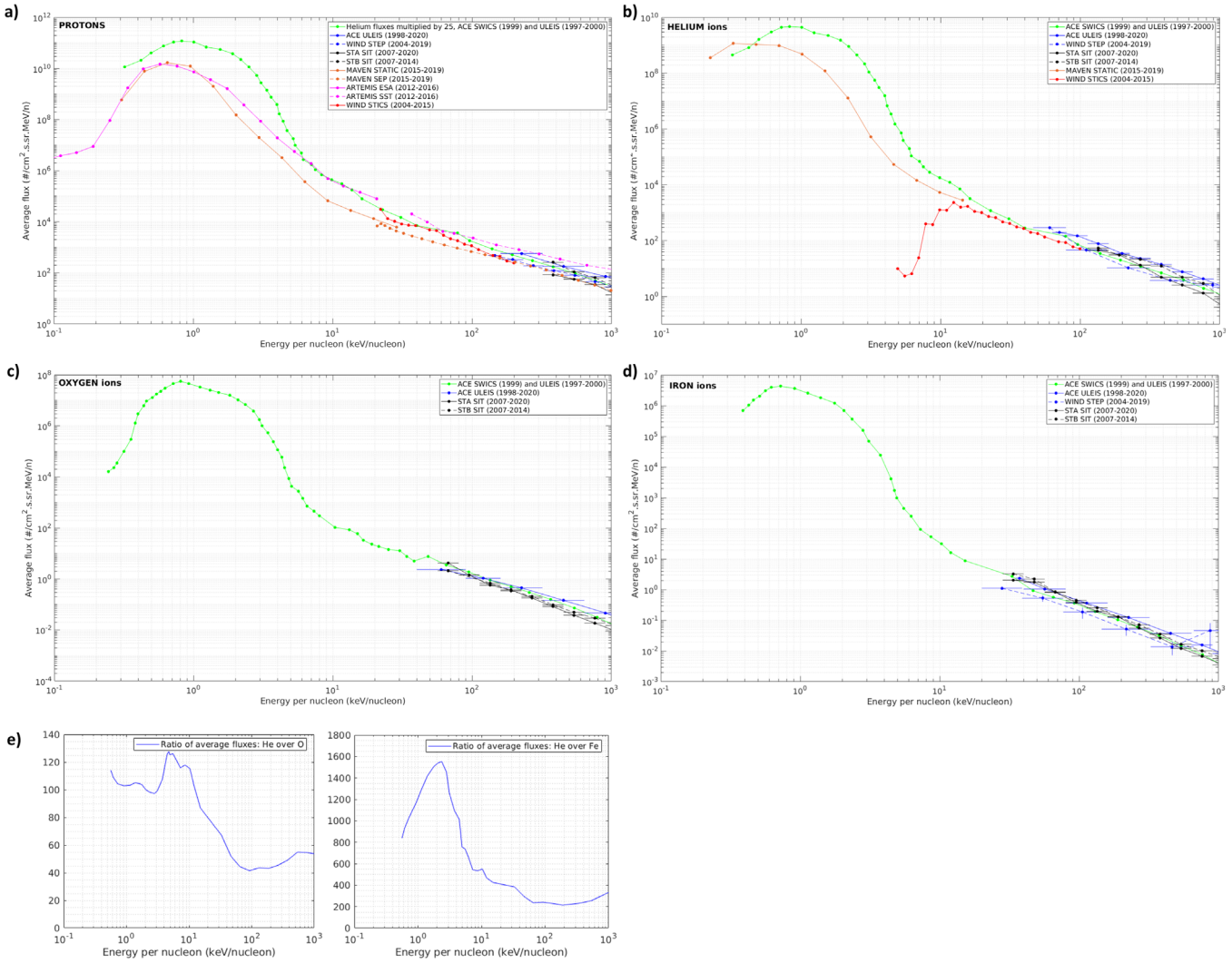

Figure 1. (a) Long-term averaged omnidirectional energy spectra of solar wind protons. Horizontal bars show the energy passbands of instrument channels. (b) Same for solar wind helium ions, including singly and doubly charged ions, except for the MAVEN-STATIC observation, which is for He^{++} only. (c) Solar wind oxygen ions. (d) Solar wind iron ions. Vertical bars show the Poisson statistics counting error and (e) ratio (no unit) of the averaged fluxes of helium ions (in units of $cm^{-2}\ s^{-1}\ sr^{-1}\ MeV^{-1}$ nucleon) over fluxes of oxygen and iron ions, from the spectra published by Mewaldt et al. (2001; green curves on Figures 1(b), (c), and (d)). The Mewaldt et al. (2001) spectra are available as supplementary data.

(The data used to create this figure are available.)

In this article, we focus on weathering effects that develop in the uppermost micrometer (1000 nm) of regolith grains or surfaces. This is motivated by the fact that sputtering occurs in the top tens of nanometers and that amorphous rims have an observed maximum thickness of ∼250 nm.

We therefore need to constrain the kinetic energy spectra of ions over the large energy range of 0.1 keV $nucleon^{-1}$ to 200 keV $nucleon^{-1}$ (see Section 4 and Figure 3(a)), which encompasses ions in the thermal and suprathermal regimes. To do so, observations gathered by electrostatic analyzers and SSD-based systems should be combined. In addition, as we focus on weathering effects that develop on long timescales, we look for estimates of ion fluxes averaged over several years. In this section, all available long-term energy spectra of protons, alphas, and solar wind minor ions are compiled (Section 2.1) and compared between each other (Section 2.2) in order to constrain as best as possible this long-term bombarding ion environment.

2.1. Compiling All Available Long-term Energy Spectra of Solar Wind Protons, Helium Ions, Oxygen Ions, and Iron Ions

All ion observations discussed hereafter are averaged over the fields of view of each instrument and are assumed to be representative of the omnidirectional ion flux. This condition is generally verified as electrostatic analyzers have large fields of view, SSD-based systems use multiple telescopes pointing in different directions, and spacecraft spin motions help to point ion instruments toward all directions of the sky (Gloeckler 2010). Omnidirectional long-term averaged energy spectra have been previously computed near the Moon and Phobos for protons and alpha particles (Poppe et al. 2018; Nénon et al. 2019), but not for minor ions and are introduced briefly before we turn our attention to the ion observations gathered by the ACE, Wind, and STEREO missions.

For protons, Poppe et al. (2018) combined the long-term observations gathered from 2012 to 2016 by the ESA and SST instruments on board the two ARTEMIS probes (magenta curves

on Figure 1(a)). Near the moon Phobos around Mars, Nénon et al. (2019) combined observations of protons and alpha particles gathered from 2015 to 2019 by the MAVEN-STATIC and MAVEN-SEP experiments (orange curves on Figure 1). However, the ARTEMIS and MAVEN ion instruments cannot distinguish the heavy minor ions of the solar wind.

The four spacecraft ACE, Wind, STEREO A, and STEREO B have operated over very extended periods of time (multiple solar cycles for ACE, Wind, and STEREO A) at a fixed distance of 1 au away from the Sun. They are equipped with advanced instruments that have continuously monitored the minor ions of the solar wind. To the best of our knowledge, Figure 1 of Mewaldt et al. (2001) gives the only published energy spectra of solar wind minor ion fluxes averaged over a long period of time that account for the thermal and suprathermal ion populations. The curves published by Mewaldt et al. (2001) are mentioned as reference spectra in the literature, for instance by Gruesbeck et al. (2015) and Allegrini et al. (2016), and are reproduced for solar wind helium, oxygen, and iron ions in Figures 1(b), (c), and (d) with the green curves. In addition, an estimate of proton fluxes is added on Figure 1(a) (green curve) by multiplying the helium fluxes by 25, which represents an average density ratio between alpha particles and protons of 4% at thermal energies. For the green curves, computed by Mewaldt et al. (2001), the thermal and suprathermal populations were observed near solar maximum from 1999 January to 1999 December (11 months) by the electrostatic analyzer SWICS on board the ACE spacecraft. At higher kinetic energies ($E_k > 30$ keV nucleon^{-1}), ion fluxes were observed by the SSD-based system ACE-ULEIS during 33 months, from 1997 October to 2000 July. This time period starts close to solar minimum, captures the ascending phase of the solar cycle, and ends near solar maximum.

The blue and black curves in Figures 1(a)–(d) show the long-term averaged kinetic energy spectra of ions observed by various SSD-based systems on board the ACE, STEREO, and Wind missions. These fluxes have been processed to Level 2 and delivered to the NASA-SPDF-OmniWeb database by the instrument teams. The long-term average energy spectra shown here were computed using the Multi-Source Spectral Plots (MSSP2) tool.[3] For the ACE and STEREO missions, we use the longest periods of time possible, whereas we only use data obtained after 2004 June for Wind, when the mission continuously stayed close to the Sun–Earth L1 libration point. In order to identify minor ions of the solar wind, high-energy instruments use double coincidence, i.e., a combined recording of deposited energies in SSDs with a measurement of the ion time of flight. They are as such not significantly sensitive to the background induced by sunlight and penetrating particles, which we assume is negligible against the ion signal.

The last publicly available data set that is of interest to characterize solar wind ions over long periods of time was acquired by the STICS electrostatic analyzer on board the Wind spacecraft and delivered for protons and alpha particles to the NASA-SPDF-CDAWeb repository. The available data set consists of triple coincidence observations (electrostatic analyzer, time of flight, SSD) and therefore has a relatively negligible background level. The omnidirectional observations gathered by the instrument were averaged from 2004 June to 2015 December, and the computed energy spectra are shown in red in Figures 1(a) and (b). It can be noted that STICS observations cover an energy range lower than SSD-based systems and therefore extend available estimates of long-term fluxes to lower energies down to around 30 keV nucleon^{-1}.

We note that the electrostatic analyzers ACE-SWICS, Wind-SWICS, and STEREO-PLASTIC have observed thermal and suprathermal ions over decades. Plasma moments that are integrated over the measured distribution function are available for the entirety of each respective mission (e.g., Lepri et al. 2013 for ACE-SWICS); however, observed energy spectra are neither validated nor publicly available and therefore cannot be used to compute the long-term averaged, differential in energy flux that this study focuses on.

2.2. Comparing Solar Wind Ion Spectra Observed by Different Instruments over Different Periods of Time

For iron ions (Figure 1(d)) with kinetic energies greater than 30 keV nucleon^{-1}, the agreement between the spectrum computed by Mewaldt et al. (2001; green curve) and the long-term observations of ACE-ULEIS, Wind-STEP, and the two STEREO-SIT experiments is remarkable, as we note that all the spectra agree with each other within a factor of 2, even if the Wind-STEP observation is a bit off. From Figure 1(d), it can be concluded that the geometric factors of each instrument are correctly estimated and that computing a long-term average of the flux spectra of >30 keV nucleon^{-1} iron ions possibly brought by transient solar wind phenomena over a period of only a few years (green curve, 1997–2000) is enough to capture the average energy spectra observed over several solar cycles by ACE, Wind, and STEREO. The same conclusion is drawn for oxygen ions (Figure 1(c)) with kinetic energies higher than 60 keV nucleon^{-1}.

For helium ions with kinetic energies greater than 10 keV nucleon^{-1}, the agreement between the spectrum of Mewaldt et al. (2001) and the ACE, Wind, and STEREO spectra is convincing. We note that the Wind-STICS energy spectrum (red curve) decreases with decreasing energy below 15 keV nucleon^{-1}. This likely comes from an overestimation of the instrument efficiency at these energies, which are close to the SSD detection threshold of 35 keV (8.75 keV nucleon^{-1}). This decrease is therefore probably unreal and should not be considered.

For the thermal and suprathermal helium ions with energies lower than 10 keV nucleon^{-1}, the long-term observation of MAVEN-STATIC (2015–2019, orange curve; Nénon et al. 2019) can be compared with the 11 month averaged spectrum observed by ACE-SWICS in 1999 (green curve). Fluxes are significantly different. First, the shoulder observed at 2 keV nucleon^{-1} in the 1999 spectrum created during fast solar wind periods (Mewaldt et al. 2001) is absent in the MAVEN observation. The fact that the solar wind was faster in 1999 than in 2015–2019 also explains that the MAVEN differential fluxes are maximum at an energy of around 0.7 keV nucleon^{-1}, which is lower than the 1 keV nucleon^{-1} of the 1999 spectrum. Finally, at thermal energies, MAVEN fluxes are a factor of 5 lower than those observed by ACE-SWICS, because the solar wind densities and bulk velocities were on average lower in 2015–2019 than in 1999.

For protons (Figure 1(a)) with kinetic energies higher than 20 keV nucleon^{-1}, there is an excellent agreement between the spectrum estimated from the helium spectrum of Mewaldt et al. (2001;green curve) and the observations of ARTEMIS, MAVEN, ACE, Wind, and STEREO. At suprathermal energies

[3] Available at https://omniweb.gsfc.nasa.gov/ftpbrowser/flux_spectr_m2.html.

of 5–10 keV nucleon^{-1}, the ARTEMIS-ESA observation and the 1999 ACE spectrum (green) are quite similar. At thermal energies ($E_k < \sim 5$ keV nucleon^{-1}), the ARTEMIS-ESA and MAVEN-STATIC fluxes are similar, whereas the 1999 ACE spectrum exhibits faster and more numerous protons than in 2012–2019.

All long-term estimates of solar wind ion spectra have therefore been compiled and compared here. We find that the work of Mewaldt et al. (2001) is the most comprehensive estimate of the long-term relative fluxes of solar wind protons, helium ions, oxygen ions, and iron ions for the purpose of quantifying the weathering of airless bodies by the thermal and suprathermal ion populations. We therefore use in the rest of the study the helium, oxygen, and iron ion spectra computed by Mewaldt et al. (2001), and the estimate of proton fluxes shown with the green curve in Figure 1(a). This section has shown that these spectra are valid at kinetic energies higher than 10 keV nucleon^{-1} when compared with longer-term observations gathered during different periods of time by ARTEMIS, MAVEN, ACE, Wind, and STEREO. At thermal and suprathermal energies, the solar wind that was observed in 1999 may be faster and denser than longer-term averages. The adopted spectra still enable a discussion of the relative importance of thermal ions of different species in weathering airless bodies.

Figure 1(e) shows the ratio of helium fluxes to oxygen and iron ion fluxes computed at each kinetic energy per nucleon. It can be noted that this ratio is lower at high kinetic energies compared with thermal energies of $\sim$1 keV/nucleon (by a factor of $\sim$2 for oxygen ions and by factor of more than 5 for iron ions). This is an intrinsic property of the solar wind which may be linked to the fact that relative minor ion densities are enhanced during solar wind events (see Killen et al. 2012 and references therein). The enhanced proportion of minor ions relative to alpha particles at high kinetic energies may increase the importance of minor ions in weathering material at depth where only high kinetic energy ions can access (see Section 4).

The contribution to airless body weathering of other heavy minor ions than oxygen and iron ions should also be estimated to study the importance of the sum of all minor ions against alpha particles and protons. At thermal energies, the six next ion species are, from highest to lowest densities in the typical thermal solar wind (Boschler 2007; Killen et al. 2012): carbon (mass of 12 amu, density of 0.68 that of oxygen ions), magnesium (14 amu, 0.10–0.15), silicon (28 amu, 0.10–0.14), neon (20 amu, 0.08–0.14), nitrogen (14 amu, 0.08–0.11), and sulfur (32 amu, 0.05). The sum of the thermal densities of these six additional ion species is therefore around 1.09–1.27 that of oxygen ions.

At kinetic energies greater than 10 keV nucleon^{-1}, Figure 5 of Mewaldt et al. (2001) shows that all minor ion energy spectra have the same power-law slope from 1997 to 2000. This figure indicates that suprathermal minor ions ($E_k >$ 10 keV nucleon^{-1}) other than oxygen and iron ions have a total flux of around 0.7 that of oxygen.

In order to take into account the effect of minor ions other than oxygen and iron ions, we assume that their effects are similar to those of oxygen ions. This assumption may be valid for ions that have a mass close to that of oxygen (16 amu) but can be questioned for silicon (28 amu) and sulfur (32 amu) ions. With this assumption, the contribution of minor ions other than oxygen and iron is equal to 1.1–1.3 the effect of oxygen ions at thermal energies and 0.7 that of oxygen at energies greater than 10 keV nucleon^{-1}.

3. Importance of the Heavy Minor Ions of the Solar Wind for the Sputtering of Airless Body Surfaces

The flux of neutral atoms sputtered from a surface by impacting ions is computed using Equation (1):

$$\text{Sputtered flux } [\text{cm}^{-2}\,\text{s}^{-1}] = \int_{E_k=0}^{+\infty} J(E_k)[\text{cm}^{-2}\,\text{s}^{-1}\,\text{eV}^{-1}] \times Y(E_k)[\text{no unit}]\,dE_k \text{ (eV)}, \quad (1)$$

where J is the differential flux of impacting ions, and Y is the sputtering yield or mean number of atoms sputtered per incident ion. The kinetic energies E_k used in the integral are the center energies of each energy bin of the fluxes published by Mewaldt et al. (2001; shown with the green circles in Figure 1), while the energy intervals dE_k are the energy bin widths.

For the ion flux J, we use ion omnidirectional fluxes (see Section 2), as done by Poppe et al. (2018) and Nénon et al. (2019). For solar wind thermal ions that form a highly anisotropic beam, the omnidirectional ion flux we use here represents the long-term averaged flux seen on most of the surface around the equator of airless bodies that spin on themselves, like the Moon. Indeed, Figure 5 of Kallio et al. (2008) shows that the thermal proton and minor ion bombardment patterns are homogeneous on most of the sunward face of the Moon around the equator (noting that the effect of lunar crustal fields is not included in this work). As the Moon spins on itself, each near-equator location is impacted by a flux averaged over a lunation equal to the averaged omnidirectional flux multiplied by π steradian. Ion fluxes become more and more isotropic with increasing ion kinetic energies, as a result of their increased gyroradii. Conclusions for ion weathering at the poles of airless bodies may be different than highlighted hereafter, as a result of the differential access of ions to polar regions, which depends on the ion specie, kinetic energy, and charge state. This investigation is left for future work.

The sputtering yield Y includes the effect of two physical mechanisms (e.g., Barghouty et al. 2011): kinetic sputtering, which results from the transfer of momentum from the impacting ion to material atoms, and potential sputtering, which is linked to the release of the potential energy stored in the multiple charge state of alpha particles and minor ions.

The determination of sputtering yields is an active area of experimental and simulation research. Nénon et al. (2019) give a thorough discussion on known uncertainties for the kinetic sputtering yields of protons, alpha particles, and oxygen ions. In particular, the existing database of measured sputtering yields is limited and does not allow us to discuss the effect of all ion species at all kinetic energies encountered in the solar wind. The determination of energy and species-dependent sputtering yields therefore relies on numerical Monte Carlo simulations.

Here, we use the SRIM software, version 2013 (Ziegler et al. 2013), to determine the kinetic sputtering yields. SRIM does not provide the capability to calculate the potential sputtering yield. The "MonoLayer Collision Step" computational mode of SRIM is used, as recommended in the tool. For each of the four considered ion species (hydrogen, helium, oxygen, and iron

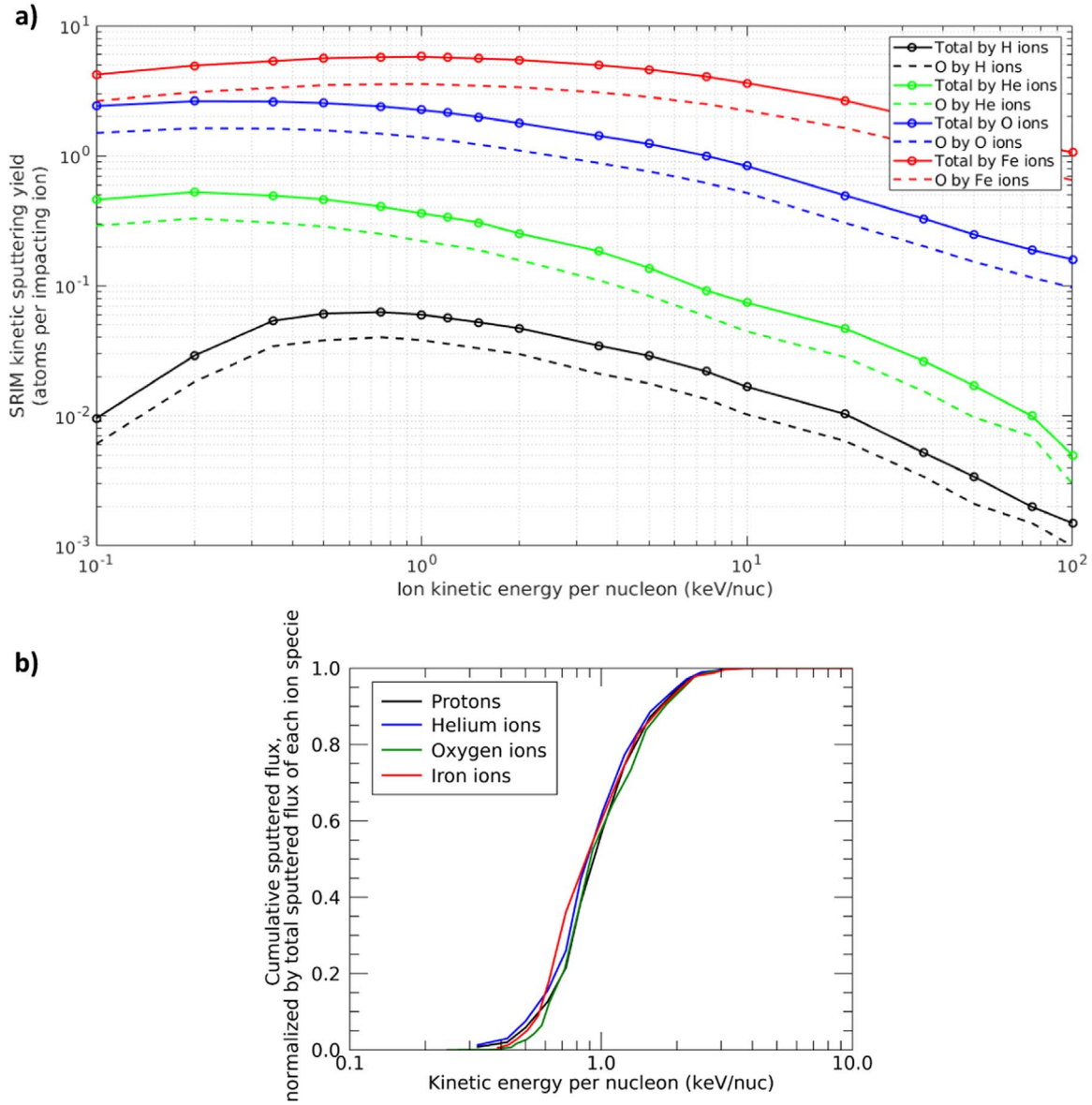

Figure 2. (a) Kinetic sputtering yields computed with SRIM for ions at normal incidence on a $MgFeSiO_4$ surface with a density of 3.8 g cc^{-1}. (b) Cumulative sputtered flux due to ions with a kinetic energy between zero and the abscissa energy, normalized by the sputtered flux due to ions at all kinetic energies.

ions), 18 SRIM simulations were conducted at logarithmically spaced energies from 100 eV $nucleon^{-1}$ to 100 keV $nucleon^{-1}$ (see circles on Figure 2(a)), so that we ran a total of 72 SRIM simulations. The sputtering yield at an energy E_k of the flux curves (green circles on Figure 1) is interpolated between the SRIM yields (circles on Figure 2(a)).

For each simulation, 100,000 ions are launched toward the surface with a normal incidence. The assumed angle of incidence is representative of a perfectly flat surface facing the solar wind thermal ion beam. Sputtering yields at higher angles of incidence are generally higher (e.g., Szabo et al. 2018). We use Fe50 olivine $MgFeSiO_4$ with a density of 3.8 g cc^{-1} as a target material, taken to have properties generally representative of the material found on airless body grains (at least on some asteroids). The surface energy, displacement energy, and lattice binding energies of this material are taken from Gray & Edmunds (2004). An important limitation of SRIM is that it is not able to account for the modification over time of the properties of the damaged layer, including the modification of atom concentrations (displaced atoms, sputtered atoms, and implanted atoms), and changes in crystal structures and bond strengths (noting that SRIM uses a structureless representation of the target material).

The validity of SRIM and the alternative software tool SDTrimSP (Mutzke et al. 2011) to compute kinetic sputtering yields at solar wind energies is an open debate (Hofsäss et al. 2014; Schaible et al. 2017; Szabo et al. 2018, 2020). For instance, Szabo et al. (2018) show that SDTrimSP better reproduces experimental measurements for the sputtering of wollastonite ($CaSiO_3$) by 2 keV Ar^+ ions than SRIM at all angles of incidence, with SRIM overestimating the sputtering yield at normal incidence by a factor of 1.4. However, Szabo et al. (2018) also report that SRIM is better suited than SDTrimSP to estimate the sputtering yield due to 2 keV H_2^+ ions (representative of two 1 keV protons) at all angles of incidence, with SDTrimSP overestimating the normal sputtering yield by a factor of 1.3. Differences between the two software outputs can be attributed to different default input parameters but may also come from different approaches for the simulations of collisions and stopping of projectiles (Szabo et al. 2018). We

Table 2
Fluxes of Atoms Sputtered from a $MgFeSiO_4$ Surface by Solar Wind Ions at Normal Incidence, Computed from the Energy-dependent Ion Fluxes of Mewaldt et al. (2001) and SRIM Kinetic Sputtering Yields

	Protons	He Ions	O Ions	Fe Ions	Minor Ions Other than O and Fe	All Ions (Only Kinetic Sputtering)
Total sputtered flux ($cm^{-2}.s^{-1}$)	$9.85\ 10^7$ (74.1% of the total)	$2.45\ 10^7$ (18.4%)	$4.39\ 10^6$ (3.30%)	$3.30\ 10^5$ (0.25%)	$5.27\ 10^6$ (3.96%)	$1.33\ 10^8$ (100%)
Surface O atoms sputtered flux ($cm^{-2}.s^{-1}$)	$6.24\ 10^7$ (74.6%)	$1.51\ 10^7$ (18.1%)	$2.70\ 10^6$ (3.23%)	$2.04\ 10^5$ (0.24%)	$3.24\ 10^6$ (3.87%)	$8.36\ 10^7$ (100%)

therefore acknowledge that the absolute values of the sputtering yields computed with SRIM and shown on Figure 2(a) for all atoms and surface oxygen atoms only can be debated; however, we use SRIM in this study to determine the relative importance of the different ion energies and species in the neutral atom sputtering process.

For the importance of different ion energies, Figure 2(b) gives the flux of atoms sputtered via only kinetic sputtering by ions with a kinetic energy per nucleon between 0 and the abscissa energy, normalized by the sputtered flux due to all kinetic energies together. Using either all sputtered atoms or only surface oxygen atoms give overlapping curves. It can be seen that, for sputtering, solar wind ions can be approximated by monoenergetic ion beams, as 80% (between 0.1 and 0.9) of the sputtered flux comes from 0.6 to 1.8 keV $nucleon^{-1}$ ions, and 50% (0.25–0.75) from 0.7–1.0 keV $nucleon^{-1}$ ions.

Regarding the role of the different ion species, Table 2 gives the flux of neutral atoms kinetically sputtered by the considered impacting ions for all surface atoms and surface oxygen atoms only. The contribution of minor ions other than oxygen and iron ions is estimated by multiplying the effect of oxygen ions by 1.2 (see Section 2). It can be noted that, for both the total sputtered flux and surface oxygen atoms alone, protons kinetically sputter around 4.0 times more atoms than alpha particles, 22.4 times more atoms than oxygen ions, and 298 times more than iron ions. Iron ions are therefore negligible for sputtering compared to oxygen ions because their slightly higher sputtering yields near 1 keV $nucleon^{-1}$ (Figure 2(a)) does not compensate for their thermal fluxes being ~20 times lower than those of oxygen ions.

Solar wind minor ions contribute to around 7.5% of the total sputtered flux computed by taking into account only kinetic sputtering. However, potential sputtering should be considered. The level at which this sputtering mechanism operates in planetary material is uncertain, but ion irradiation experiments show that it may increase the flux of neutral atoms sputtered from lunar-type soils by alphas and minor ions by a factor of at maximum 2 (Barghouty et al. 2011; Killen et al. 2012; Szabo et al. 2018, 2020). By multiplying the effect of these ions by 2, the contribution of minor ions to total sputtering is of 12%. If potential sputtering of alpha particles is assumed small compared to the potential sputtering of more highly charged minor ions, the minor ion contribution increases to 14%. Solar wind minor ions heavier than alpha particles are therefore found here to be responsible for 8% to 14% of the total sputtering of airless body surfaces. This result relies on a new approach, which is to combine the 11 month averaged energy spectra published for thermal ions by Mewaldt et al. (2001) with the relative kinetic sputtering yields of one ion species to another, computed with SRIM at normal incidence. It highlights that trace ions in the solar wind are neither minor nor negligible at sputtering airless bodies over long periods of time. Any experiment or modeling effort that investigates the long-term effects of sputtering should therefore consider the minor ions of the solar wind, as reported for transient and dynamic sputtering by Barghouty et al. (2011), Killen et al. (2012), and Szabo et al. (2018, 2020).

4. Importance of Solar Wind Minor Ions in Weathering Airless Body Surfaces at Depth

In Section 3, atomic displacements induced close to the surface by thermal solar wind minor ions have been shown to significantly contribute to sputtering. We investigate hereafter the importance of suprathermal ions in altering the material at depths greater than the penetration depth of thermal ions. This effort is motivated by the fact that Section 2 and Figure 1(e) highlight that the ratio of minor ion fluxes to helium ion fluxes increases with increasing kinetic energy, which may enhance the relative importance of minor ions at suprathermal energies, compared with the situation at thermal energies.

The number of atomic displacements generated per time unit (atomic displacement production rate) by impacting ions is computed with the SRIM software as a function of depth inside the material using the input parameters detailed in Section 3. The objective is to study the relative importance of the different ion energies and species in altering the crystallinity of the material as a function of depth (Poppe et al. 2018). It should be noted that the computation of atomic displacements with SRIM relies on the unconstrained displacement energy parameter of each material atom, so that the absolute value of the computed number of atomic displacements is meaningless. However, SRIM can be used to study the relative importance of different ion energies and species for this process (Christoffersen & Keller 2011). As noted by Christoffersen & Keller (2011), another output of SRIM can be used as a proxy to study the capability of ions to induce atomic displacements: the deposited nuclear-elastic collisional energy. Using this output instead of atomic displacements, we reach the same quantitative conclusions regarding the importance of solar wind minor ions relative to protons and alphas in inducing atomic displacements.

The material starts to become amorphous at a given depth below the surface when the concentration of ion-generated defects at that depth, in the form of atomic displacements or other extended defects, reaches a critical level. This concentration accordingly depends on the irradiated fluence, and the rate at which the crystal approaches this critical concentration depends on the irradiated flux. Overall, the net rate of defect accumulation (as a measure of progress toward amorphization) is a function of the rate of defect accumulation counterbalanced by the rate at which dynamic recovery and thermally assisted diffusion processes remove defects (Christoffersen et al. 2020 and references cited therein).

Figure 3(a) shows the production rate of atomic displacements created by an individual impacting ion, as a function of

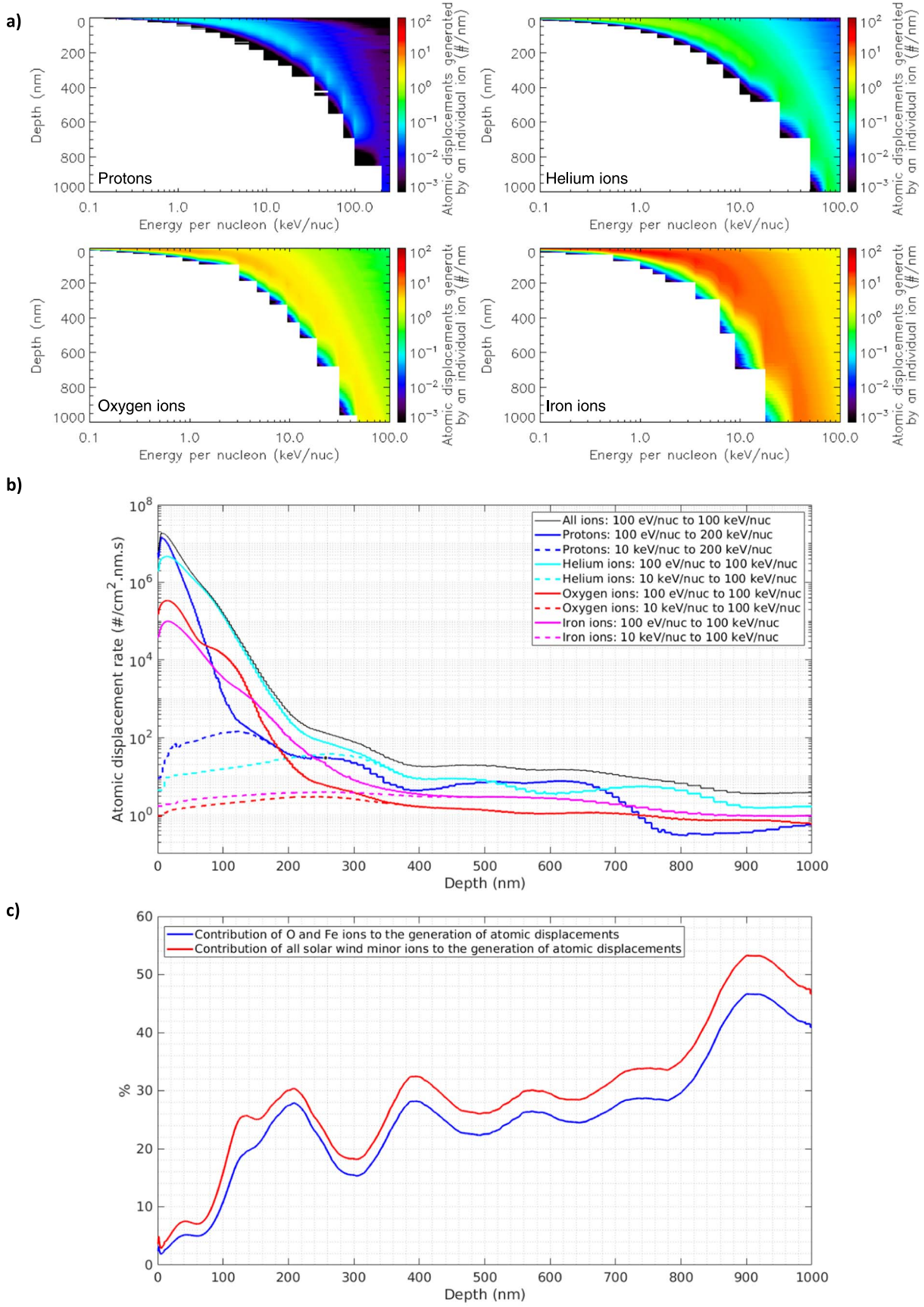

Figure 3. (a) Number of atomic displacements induced by an individual impacting ion, as a function of its species, kinetic energy, and depth in the material. (b) Atomic displacement rate computed by convolving the effect of an individual ion (Figure 3(a)) with the long-term averaged ion energy spectra of Mewaldt et al. (2001). The "All ions" curve shows the sum of the effect of protons, alphas, oxygen, and iron ions but does not account for other minor ion species (see text). (c) Contribution percentage of solar wind minor ions to the generation of atomic displacements as a function of depth in the material.

its species, its kinetic energy, and the depth inside the material. As seen on Figure 3(a), using kinetic energy per nucleon up to 200 keV nucleon^{-1} for protons and 100 keV nucleon^{-1} for other ion species is sufficient to correctly compute atomic displacements created in the uppermost micrometer of the material. SRIM does not account for the effects linked to the multiple charge state of alpha particles and minor ions (which create the potential sputtering), so that the rates of atomic displacements may be higher than shown here for ions with kinetic energies that are small compared to the ion potential energy (maybe lower than 25 keV nucleon^{-1}; Barghouty et al. 2011; Killen et al. 2012).

At each depth inside the material and for each ion species, we convolve (integral over kinetic energies) the number of atomic displacements created by a single ion (the SRIM output) with the long-term averaged ion fluxes. To do so, the number of atomic displacements created at a given depth by a single ion with a kinetic energy equal to the center energy of an ion flux measurement bin (green circles on Figure 1) is interpolated in the SRIM results. The energy bins shown in Figure 1 are small enough so that we can assume that the number of displacements created by the center energy of each bin is representative of the number of displacements created by any other kinetic energy in the bin. The solid lines on Figure 3(b) show the atomic displacement rates, computed by convolving the effect of a single ion with the ion energy spectra given by Mewaldt et al. (2001, green curves on Figure 1), integrated over all kinetic energies higher than 0.1 keV nucleon^{-1}. The dashed lines isolate the contribution of >10 keV nucleon^{-1} ions, for which the energy spectra are very well constrained by the long-term ion measurements of ACE, Wind, and STEREO (see Section 2). The blue curve in Figure 3(c) gives the sum of the contributions (in percent) of minor oxygen and iron ions to the total rate of atomic displacements. Other minor ion species are considered by adding 0.7 of the effect of oxygen ions (see Section 2), and the red curve gives the total contribution of minor ions.

In the uppermost tens of nanometers, the contribution of solar wind minor ions to the displacement of material atoms may appear relatively small (∼5%), but it could possibly be enhanced by the minor ion potential energy, as for potential sputtering (Section 3).

Deeper than 400 nm, atomic displacements are induced by only >10 keV nucleon^{-1} ions (Figure 3(a)), for which the long-term averaged fluxes are well constrained. The total rate of atomic displacements at these depths (black solid line on Figure 3(b)) is six orders of magnitude slower than at 10 nm and four orders of magnitude slower than at 100 nm. Airless body material at depths greater than 400 nm may have therefore not been exposed long enough to solar wind ions, as a result of surface refreshing processes, to receive the minimum amorphization critical fluence (Carrez et al. 2002), which explains the observation that amorphous rims are generally thinner than 250 nm. Still, minor ions create 25%–50% of the total number of atomic displacements at depths greater than 400 nm, as a result of their greater natural abundances relative to protons and helium ions at suprathermal kinetic energies than at thermal energies (see Section 2 and Figure 1(e)). Heavy minor ions of the solar wind therefore are a controlling factor in allowing ion damage processes to continue to proceed at depths greater than 400 nm. The rate at which damage occurs at these greater depths is therefore not zero but appreciable enough so that at sufficiently long exposure times, amorphization might extend to these greater depths, resulting in the continued widening of amorphized rims.

The red curve in Figure 3(c) shows that heavy minor ions are also likely important at disordering the material at depths between 100 and 400 nm. This conclusion is drawn by using the suprathermal ion spectra published by Mewaldt et al. (2001), which relies on observations gathered over 11 months by the ACE-SWICS instrument in 1999. As detailed in Section 2, ion fluxes at these energies (∼0.2–10 keV nucleon^{-1}) and for the four species of interest cannot be validated against other long-term observations. Nevertheless, these results indicate that it is likely that heavy minor ions significantly participate in the creation of amorphous rims with thicknesses <250 nm, by creating more than 20% of atomic displacements in the originally crystalline material.

5. Summary and Discussion

In Section 2, all available observations of long-term average energy spectra of solar wind protons, helium ions, oxygen ions, and iron ions impacting airless bodies were compiled. The energy spectra published for thermal and suprathermal ions by Mewaldt et al. (2001) are found to be the most comprehensive data set available to date to investigate the importance of minor ions at most kinetic energies encountered in the solar wind for the weathering of airless bodies. The spectra of >10 keV nucleon^{-1} ions published by Mewaldt et al. (2001) are generally consistent and validated against longer-term observations gathered over years or decades by particle instruments on board the ACE, Wind, STEREO A, STEREO B, ARTEMIS, and MAVEN spacecraft. We therefore recommend the use of the Mewaldt et al. (2001) spectra to ion weathering modelers and experimentalists. The associated flux values scanned from the 2001 paper are made available in a supplementary data file together with indications to convert differential fluxes to ion fluxes in cm^{-2}.s^{-1}. In particular, the oxygen ion spectrum can be used to reconsider the contamination of lunar soils by solar wind oxygen ions as a function of depth in the material (e.g., Ireland et al. 2006). Over long periods of time, the relative abundance of solar wind minor ions over protons and helium ions is found to be higher in the suprathermal regime than at thermal energies of 1 keV nucleon^{-1}.

The long-term sputtering that occurs in the uppermost layers of regolith grains or surfaces was investigated in Section 3 by combining the ion energy spectra of Mewaldt et al. (2001) with energy-dependent sputtering yields computed at normal incidence with the SRIM software. The results of this approach indicate that minor ions of the solar wind are responsible for 8% to 14% of the total sputtered flux averaged over long timescales, as a result of the balance between ion relative fluxes, kinetic sputtering yields, and the effect of potential sputtering. Solar wind minor ions should therefore be considered to understand the long-term alteration of airless bodies by ion sputtering. Subsequently, solar wind minor ions significantly contribute to atomic displacements and material amorphization in the uppermost tens of nanometers of the material.

Our conclusion regarding the considerable role of solar wind minor ions for the long-term sputtering of airless bodies can be used to reassess the findings of a previous study which neglected their effect at the moon Phobos around Mars (Nénon et al. 2019) This small moon is not only altered by solar wind ions, but also by singly charged ions escaping the atmosphere

of the red planet. Nénon et al. (2019) pointed out that Martian ions contribute to ∼30% of the total long-term sputtering of Phobos' surface, but neglected the effect of the solar wind minor ions. Here, we can reevaluate that Martian ions contribute to in fact ∼25% of the total sputtering, which does not modify the qualitative conclusion regarding the importance of planetary ions in processing Phobos' surface.

Finally, in Section 4, the rate at which atomic displacements are induced by suprathermal ions was computed as a function of depth in the top micrometer of the material. Solar wind minor ions heavier than alpha particles were found to significantly process the material at depths greater than 100 nm, as they are responsible for 20% to 50% of the total number of displacements.

The conclusions highlighted here on the effects of thermal and suprathermal minor ions would benefit from future efforts that would average energy spectra over a longer period than the 11 months of Mewaldt et al. (2001). The ion spectra data set gathered by the ACE-SWICS, Wind-SWICS, and STEREO-PLASTIC experiments would be powerful for this endeavor; however, they are neither validated nor publicly available at this time.

The results presented here in the ecliptic plane at a distance of 1 au from the Sun apply to any planetary body with an orbit crossing this region, including the Moon and near-Earth objects. In order to extend this to all planetary bodies in the solar system, from Mercury to Pluto, the long-term abundance of minor ions and their long-term averaged energy spectra should be compiled at different distances from the Sun. In particular, the importance in the outermost heliosphere of singly charged interstellar pickup ions compared to solar wind ions could be investigated (e.g., Swaczyna et al. 2019). At a distance of 5.2 au, the Ulysses spacecraft completed three polar orbits around the Sun over 20 years and was equipped with ion instruments able to observe the thermal and suprathermal minor ions of the solar wind (e.g., Von Steiger & Zurbuchen 2006). Ulysses spent an approximate total time of less than a few years at low solar latitudes relevant for the weathering of planetary bodies near the ecliptic plane. However, energy spectra averaged over only a few years are valuable inputs for the study of ion weathering (this article; Poppe et al. 2018; Nénon et al. 2019), so that future work may combine energy spectra of minor ions observed near the ecliptic plane by Ulysses at larger heliocentric distances. Near Mercury, solar wind minor ions were observed with the Fast Imaging Plasma Spectrometer on board the MESSENGER spacecraft; however, instrumental limitations make the estimation of ion densities complex (Raines et al. 2011; Gershman et al. 2012). Nevertheless, future work may investigate whether reliable long-term ion energy spectra may be computed at a distance of 0.5 au from the Sun.

Q.N. and A.R.P. acknowledge funding from the DREAM2 and LEADER teams of NASA's Solar System Exploration Research Virtual Institute (SSERVI), with, respectively, grants NNX14AG16A and 80NSSC20M0060.

All ion observation data used in the article are publicly available in the NASA-SPDF-OmniWeb (https://omniweb.gsfc.nasa.gov/) and NASA-SPDF-CDAWeb (https://cdaweb.gsfc.nasa.gov/index.html/) repositories.

We acknowledge the MSSP2 tool (https://omniweb.gsfc.nasa.gov/ftpbrowser/flux_spectr_m2.html, PI: J. F. Cooper) and the SRIM software (http://www.srim.org/, PI: J. Ziegler) used in this article.

We thank J. Raines (University of Michigan) for discussions on ACE-SWICS and Wind-STICS data availability. We also thank J. Luhmann (U.C. Berkeley) and A. Galvin (University of New Hampshire) for discussions on the availability of STEREO-PLASTIC data. Finally, we are thankful to R. Mewaldt (Caltech) for discussions on his 2001 work and publication.

ORCID iDs

Quentin Nénon https://orcid.org/0000-0001-8130-9832
Andrew R. Poppe https://orcid.org/0000-0001-8137-8176

References

Acuña, M. H., Ogilvie, K. W., Baker, D. N., et al. 1995, SSRv, 71, 5
Adriani, O., Barbarino, G. C., Bazilevskaya, G. A., et al. 2011, Sci, 332, 69
Allegrini, F., Ho, G. C., Desai, M. I., et al. 2016, JGRA, 121, 11,637
Angelopoulos, V. 2011, SSRv, 165, 3
Barghouty, A. F., Meyer, F. W., Harris, et al. 2011, NIMPB, 269, 1310
Bibring, J. P., Duraud, J. P., Durrieu, L., et al. 1972, Sci, 175, 753
Bochsler, P. 2007, A&ARv, 14, 1
Brunetto, R., & Strazzulla, G. 2005, Icar, 179, 1
Carrez, P., Demyk, K., Cordier, P., et al. 2002, M&PS, 37, 1599
Christoffersen, R., & Keller, L. P. 2011, M&PS, 46, 950
Christoffersen, R., & Keller, L. P. 2015, LPSC, 46, 2084
Christoffersen, R., Keller, L. P., & Dukes, C. 2020, LPSC, 51, 2147
Christoffersen, R., McKay, D. S., & Keller, L. P. 1996, M&PS, 31, 835
Dran, J. C., Durrieu, L., Jouret, C., et al. 1970, E&PSL, 9, 391
Elphic, R. C., Funsten, H. O., III, Barraclough, B. L., et al. 1991, GeoRL, 18, 2165
Fisk, L. A., & Gloeckler, G. 2008, ApJ, 686, 1466
Galvin, A. B., Kistler, L. M., Popecki, M. A., et al. 2008, SSRv, 136, 437
Gershman, D. J., Zurbuchen, T. H., Fisk, L. A., et al. 2012, JGRA, 117, A00M02
Gloeckler, G. 2003, in AIP Conf. Proc. 679, Solar Wind Ten (Melville, NY: AIP), 583
Gloeckler, G. 2010, in Heliophysics: Space Storms and Radiation: Causes and Effects, ed. C. J. Schrijver & G. L. Siscoe (London: Cambridge Univ. Press), 43
Gloeckler, G., Balsiger, H., Bürgi, A., et al. 1995, SSRv, 71, 79
Gloeckler, G., Cain, J., & Ipavich, F. M. 1998, SSRv, 86, 497
Gray, M. D., & Edmunds, M. G. 2004, MNRAS, 349, 491
Grimberg, A., Baur, H., Bochsler, P., et al. 2006, Sci, 314, 1133
Gruesbeck, J. R., Lepri, S. T., Zurbuchen, T. H., et al. 2015, ApJ, 799, 57
Hashizume, K., Chaussidon, M., Marty, B., & Robert, F. 2000, Sci, 290, 1142
Hofsäss, H., Zhang, K., & Mutzke, A. 2014, ApSS, 310, 134
Ireland, T. R., Holden, P., Norman, M. D., et al. 2006, Natur, 440, 776
Jakosky, B. M., Lin, R. P., Grebowsky, J. M., et al. 2015, SSRv, 195, 3
Kaiser, M. L., Kucera, T. A., Davila, J. M., et al. 2008, SSRv, 136, 5
Kallio, E., Wurz, P., Killen, R., et al. 2008, P&SS, 56, 1506
Keller, L. P., & McKay, D. S. 1997, GeCoA, 61, 2331
Keller, L. P., & Zhang, S. 2015, in Space Weathering of Airless Bodies: An Integration of Remote Sensing Data, Laboratory Experiments and Sample Analysis Workshop *(Houston, TX)*, 2056
Killen, R. M., Hurley, D. M., & Farrell, W. M. 2012, JGRE, 117, E00K02
Kollmann, P., Hill, M. E., McNutt, R. L., Jr., et al. 2019, ApJ, 876, 46
Larson, D. E., Lillis, R. J., Lee, C. O., et al. 2015, SSRv, 195, 153
Lepri, S. T., Landi, E., & Zurbuchen, T. H. 2013, ApJ, 768, 94
Loeffler, M. J., Dukes, C. A., & Baragiola, R. A. 2009, JGRE, 114, E03003
Luhmann, J. G., Curtis, D. W., Lin, R. P., et al. 2005, AdSpR, 36, 1534
Marchi, S., Brunetto, R., Magrin, S., et al. 2005, A&A, 443, 769
Mason, G. M., Gold, R. E., Krimigis, S. M., et al. 1998, In The Advanced Composition Explorer Mission (Dordrecht: Springer)
McFadden, J. P., Carlson, C. W., Larson, D., et al. 2008, SSRv, 141, 277
McFadden, J. P., Kortmann, O., Curtis, D., et al. 2015, SSRv, 195, 199
Mewaldt, R. A., Mason, G. M., Gloeckler, G., et al. 2001, in AIP Conf. Proc. 598, Solar and Galactic Composition: A Joint SOHO/ACE Workshop (Melville, NY: AIP), 165
Möbius, E., Hovestadt, D., Klecker, B., et al. 1985, Natur, 318, 426
Mutzke, A., Schneider, R., & Dohmen, R. 2011, SDTrimSP version 5.00 (Garching bei München: Max-Planck-Institut für Plasmaphysik), https://pure.mpg.de/rest/items/item_2139848_1/component/file_2139847/content
Nénon, Q., Poppe, A. R., Rahmati, A., et al. 2019, JGRE, 124, 3385

Noguchi, T., Kimura, M., Hashimoto, et al. 2014, M&PS, 49, 188
Ozima, M., Seki, K., Terada, N., et al. 2005, Natur, 436, 655
Pieters, C. M., & Noble, S. K. 2016, JGRE, 121, 1865
Poppe, A. R., Farrell, W. M., & Halekas, J. S. 2018, JGRE, 123, 37
Raines, J. M., Slavin, J. A., Zurbuchen, T. H., et al. 2011, P&SS, 59, 15
Sanchez, J. A., Reddy, V., Nathues, A., et al. 2012, Icar, 220, 1
Schaible, M. J., Dukes, C. A., Hutcherson, A. C., et al. 2017, JGRE, 122, 1968
Shemansky, D. E. 2003, in AIP Conf. Proc. 663, Rarefied Gas Dynamics: 23rd International Symp., ed. A. D. Ketsdever & E. P. Muntz (Melville, NY: AIP), 687
Stone, E. C., Frandsen, A. M., Mewaldt, R. A., et al. 1998, SSRv, 86, 1
Swaczyna, P., McComas, D. J., & Zirnstein, E. J. 2019, ApJ, 875, 36
Szabo, P. S., Biber, H., Jäggi, N., et al. 2020, ApJ, 891, 100
Szabo, P. S., Chiba, R., Biber, H., et al. 2018, Icar, 314, 98
Terada, K., Yokota, S., Saito, Y., et al. 2017, NatAs, 1, 0026
Von Rosenvinge, T. T., Barbier, L. M., Karsch, et al. 1995, SSRv, 71, 155
Von Steiger, R., Schwadron, N. A., Fisk, L. A., et al. 2000, JGR, 105, 27217
Von Steiger, R., & Zurbuchen, T. H. 2006, GeoRL, 33, L09103
Weber, W. J., & Zhang, Y. 2019, COSSM, 23, 100757
Wurz, P., Whitby, J. A., Rohner, U., et al. 2010, P&SS, 58, 1599
Ziegler, J. F., Biersack, J. P., & Ziegler, M. D. 2013, Srim-2013 (Stopping and Range of Ions in Matter)